Squaring the Circle: Geometric Skewness and Symmetry Breaking for Passive Scalar Transport in Ducts and Pipes

Manuchehr Aminian,[*] Francesca Bernardi,[†] Roberto Camassa,[‡] and Richard M. McLaughlin[§]
Department of Mathematics, University of North Carolina, Chapel Hill, North Carolina 27599, USA
(Received 2 June 2015; published 5 October 2015)

We study the role geometry plays in the emergence of asymmetries in diffusing passive scalars advected by pressure-driven flows in ducts and pipes of different aspect ratios. We uncover nonintuitive, multi-time-scale behavior gauged by a new statistic, which we term "geometric skewness" $\mathcal{S}^{\mathcal{G}}$, which measures instantaneously forming asymmetries at short times due to flow geometry. This signature distinguishes elliptical pipes of any aspect ratio, for which $\mathcal{S}^{\mathcal{G}} = 0$, from rectangular ducts whose $\mathcal{S}^{\mathcal{G}}$ is generically nonzero, and, interestingly, shows that a special duct of aspect ratio ≈ 0.53335 behaves like a circular pipe as its geometric skewness vanishes. Using a combination of exact solutions, novel short-time asymptotics, and Monte Carlo simulations, we establish the relevant time scales for plateaus and extrema in the evolution of the skewness and kurtosis for our class of geometries. For ducts limiting to channel geometries, we present new exact, single-series formulas for the first four moments on slices used to benchmark Monte Carlo simulations.

DOI: 10.1103/PhysRevLett.115.154503 PACS numbers: 47.51.+a, 05.40.-a, 47.60.Dx, 47.85.lk

Introduction.—Taylor dispersion quantifies the long-time effective longitudinal diffusion of a tracer advected by a steady shear flow [1]. The result for a circular pipe is $\kappa_{\text{eff}} = \kappa[1 + (\hat{a}^2 U^2/192\kappa^2)]$, where $\hat{a}$, U, and κ are the radius of the circular cross section, characteristic velocity, and molecular diffusivity, respectively. Describing the tracer evolution well before the diffusion time scale $t = \mathcal{O}(\hat{a}^2/\kappa)$ is more challenging. Here, the distribution is both greatly non-normal and strongly spatially structured. Additionally, understanding the cross-sectional geometric influence is a physically relevant problem. There are many results for both channel and circular pipe, for point-source [2–4], uniform plug [2,3,5–8], and other initial conditions [4,9]. Considerably less is known for intermediate time scales in the duct or for more general geometries.

The simplest case is the channel with a transversely uniform initial condition. Even this is not trivial. While the solution and its moments can be calculated via Green's function or eigenfunction expansion, it can be difficult to extract useful information directly from these due to nested integrals or multiple series.

Here, we focus on the evolution of the skewness in different geometries to understand symmetry breaking. The skewness, the centered normalized third moment, is the lowest-order statistic of a distribution whose sign identifies asymmetry due to the slowest tail decay being on the left (negative) or right (positive) side of the mean. Characterizing asymmetric effects may play important roles over scales from drug delivery via capillary blood flow [10], to the distribution of contaminants in rivers and estuaries [11], and is potentially relevant in understanding the motion of organisms driven by chemotaxis [12].

In this Letter, we document new phenomena and develop new mathematical techniques to provide quantitative predictions. In the process, we introduce a new concept we term *geometric skewness* $\mathcal{S}^{\mathcal{G}}$ measuring the interplay between geometry and flow in breaking the symmetry of the distribution, even in the absence of diffusion.

For uniform initial data in the channel, we use the Aris [13] moment hierarchy to derive, for the first time, single-series formulas for the first three moments along streamwise slices (henceforth, "partial" moments), as well as their cross-sectionally averaged counterparts through the fourth moment ("full" moments). We then implement Monte Carlo simulations validated against our exact channel solutions. In turn, we explore the dependence of the moments on Péclet number and cross-sectional geometry in more complex domains, focusing on three cases: channel, elliptical pipe, and rectangular duct parametrized by $\lambda = a/b$, the aspect ratio of short to long half-sides. To explain numerically observed phenomena, we derive short-time asymptotics in generic domains with a new methodology developed below.

We next apply our asymptotics for large Péclet number, for which the full skewness plateaus at the value of the geometric skewness $\mathcal{S}^{\mathcal{G}}$, at a time scale a/U. We discuss the ordering of this and other known time scales in the large Péclet regime.

Advection-diffusion equation and geometries.—The tracer density $T(\mathbf{x}, t)$ evolves according to the advection-diffusion equation with diffusivity κ:

$$\partial_t T + \tilde{u}\partial_x T = \kappa(\partial_x^2 + \mathcal{L})(T). \tag{1}$$

Here, $T(\mathbf{x}, 0) = f(x)$, $\partial_{\mathbf{n}} T|_{\partial\Omega} = 0$, $\mathbf{x} = x\mathbf{i} + y\mathbf{j} + z\mathbf{k}$ is the coordinate system in $\mathbb{R}^3$, $\tilde{\boldsymbol{u}}(\mathbf{x}) = \tilde{u}(y, z)\mathbf{i}$ is the fluid velocity, and the initial data $f(x)$ a symmetric function with variance σ^2 and taken to be a Dirac delta $\delta(x)$

(uniform in y and z) unless otherwise stated; the boundary conditions are zero flux on $\partial\Omega$ with outward normal $\mathbf{n}$, and Ω is the cross-sectional domain perpendicular to $\mathbf{i}$; finally, $\mathcal{L} = \partial_y^2 + \partial_z^2$.

The flows are steady-state solutions to the Navier-Stokes equations $\mathcal{L}(\tilde{u}) = 2p_x/\mu$ with a constant pressure gradient $\nabla p = p_x\mathbf{i}$, $p_x < 0$, with viscosity μ and no-slip boundary conditions (factor 2 is for convenience). Simple solutions for channel and ellipse exist, while the duct requires eigenfunction expansion [14].

In the mean velocity frame, denoting $u = \tilde{u} - \langle\tilde{u}\rangle$, where $\langle\cdot\rangle$ is the area mean over Ω, system (1) retains the same form with flow u instead of $\tilde{u}$. With nondimensionalized $\mathbf{x}'$ and τ as $\mathbf{x}' = \mathbf{x}/a$ and $\tau = (\kappa/a^2)t$ with Péclet number $\mathrm{Pe} = Ua/\kappa$, using characteristic velocity $U = a^2|p_x|/\mu$ based on a fixed pressure gradient, and immediately dropping the primes (alternative nondimensionalizations discussed below), the partial moments $T_n = \int_{\mathbb{R}} dx\, x^n\, T(\mathbf{x}, t)$ obey [13]

$$\partial_\tau T_n - \mathcal{L}(T_n) = n(n-1)T_{n-2} + \mathrm{Pe}u(\mathbf{x})nT_{n-1}, \quad (2)$$

with $T_n(y, z, 0) = \int_{\mathbb{R}} dx\, x^n f(x)$, $\partial_{\mathbf{n}} T_n|_{\partial\Omega} = 0$, and $n = 0$, $1, \ldots, T_{-2} = T_{-1} = 0$.

The full moments are $\mathcal{M}_n \equiv \int_{\mathbb{R}} dx x^n \langle T(x, y, z, \tau)\rangle$. The partial skewness (kurtosis) is the centered third (fourth) partial moment normalized by its standard deviation to the third (fourth) power, and similarly for the full quantities.

Exact solutions in the channel.—For the channel, the first three partial moments and full fourth moment for Eq. (1) have the following *single-series* solutions:

$$\begin{aligned}
T_1(y,\tau) &= \mathrm{Pe}\mathcal{P}_1(y,\tau) + \mathrm{Pe}\sum_{n=1}^{\infty}\mathcal{P}_2(y,\tau;n)\cos(n\pi y),\\
T_2(y,\tau) &= \sigma^2 + 2\tau + \mathrm{Pe}^2\mathcal{Q}_1(y,\tau)\\
&\quad + \mathrm{Pe}^2\sum_{n=1}^{\infty}[\mathcal{Q}_2(y,\tau;n)\cos(n\pi y)\\
&\quad + \mathcal{Q}_3(y,\tau;n)\sin(n\pi y)],\\
T_3(y,\tau) &= \mathrm{Pe}\mathcal{R}_1(y,\tau) + \mathrm{Pe}\sum_{n=1}^{\infty}\mathcal{R}_2(y,\tau;n)\cos(n\pi y)\\
&\quad + \mathrm{Pe}^3\sum_{n=1}^{\infty}[\mathcal{R}_3(y,\tau;n)\cos(n\pi y)\\
&\quad + \mathcal{R}_4(y,\tau;n)\sin(n\pi y)]\\
&\quad + \mathrm{Pe}^3\mathcal{R}_5(y,\tau) + 3\sigma^2 T_1(y,\tau),\\
\mathcal{M}_4(\tau) &= f_4 + \sum_{n=1}^{\infty}[\mathrm{Pe}^2\mathcal{S}_1(\tau;n) + \mathrm{Pe}^4\mathcal{S}_2(\tau;n)]\\
&\quad + 12\tau^2 + \mathrm{Pe}^2\mathcal{S}_3(\tau) + \mathrm{Pe}^4\mathcal{S}_4(\tau) + 6\sigma^2\mathcal{M}_2(\tau),
\end{aligned} \quad (3)$$

where $\mathcal{P}_j$, $\mathcal{Q}_j$, $\mathcal{R}_j$, and $\mathcal{S}_j$ depend on τ, y, and n [15], where σ^2 is the variance of $f(x)$ and f_4, the fourth moment.

These formulas are new; in previous work [3], double-series formulas exist for the second partial moment, whereas here the first three partial moments are single series. We stress that these formulas arise through extremely lengthy complex residue calculations subsequently verified by symbolic manipulators. Direct calculations show that for any y, the partial skewness becomes strictly negative at long time, whereas for short time, near the boundaries, it is positive, indicating a time scale of global sign definiteness.

Simulations.—Monte Carlo simulations yield the tracer distribution evolution for general geometries. The stochastic process $d\mathbf{X}(\tau) = \mathrm{Pe}\,\boldsymbol{u}(\mathbf{X}(\tau))d\tau + \sqrt{2}d\mathbf{W}(\tau)$ yields Eq. (1). Here, $d\mathbf{W}(\tau)$ is uncorrelated $\mathbb{R}^3$ Wiener increments with reflecting boundaries on $\partial\Omega$. Simulations performed with 10^6 particles distributed according to $f(x)$ in Eq. (1). Euler-Maruyama time stepping is used with a time step $\Delta\tau \le 10^{-3}$ to compute the statistics $T_n(y, z, \tau)$, $\mathcal{M}_n(\tau)$. The duct flow is computed summing the largest 2048 Fourier modes. The Gaussian random increments $d\mathbf{W}$ are generated with the Mersenne Twister [16] and polar method [17]. Statistics are averaged over 100 independent realizations, for 10^8 sample paths. Numerics are validated against channel exact moments (Fig. 1) with uniform agreement and absolute error $\le 10^{-4}$, over ten diffusive time scales, consistent with the law of large numbers.

Figure 2 shows the duct ($\lambda = 0.2$) full skewness: multiple minima arise not present in the channel case. Negative skewness is seen in the right columns because tracer particles reach farther to the left than to the right from the mean ($x = 0$). Figure 3 depicts the skewness for varying Péclet number at fixed aspect ratio. Two minima emerge: one migrating towards $\tau = 0$, the other at a fixed time scale, for increasing Péclet number. (Similar behavior occurs for point-source initial data in future work.) Possible physical time scales

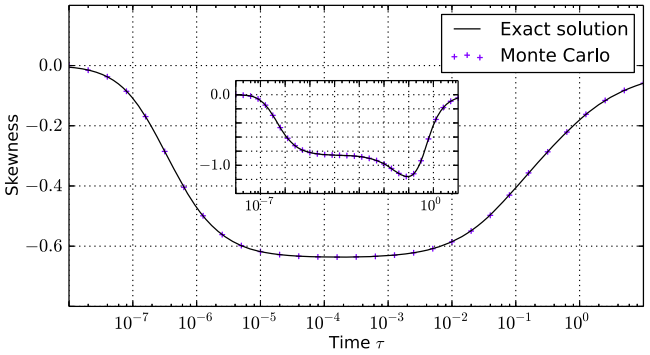

FIG. 1 (color online). Channel full skewness and kurtosis (inset) exact solutions versus Monte Carlo computations, $\mathrm{Pe} = 10^4$.

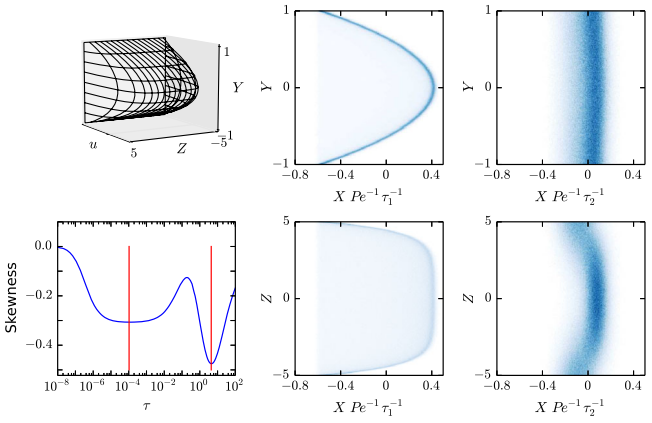

FIG. 2 (color online). Mean-zero flow profile $u(y,z)$ and full skewness (left) for duct (aspect ratio $\lambda = 0.2$, $\mathrm{Pe} = 10^4$), with snapshots of the xy and xz projections of a sample path at times marked by red lines in the skewness graph: $\tau = 10^{-4}$ (center) and $\tau = 4.4$ (right).

affecting this are κ/U^2, a/U, b/U, a^2/κ, ab/κ, b^2/κ. For large Péclet numbers, some time scales are ordered: $\kappa/U^2 < a/U < a^2/\kappa < ab/\kappa < b^2/\kappa$. Time scales corresponding to skewness features are revealed by new asymptotic analysis predicting the first plateau at time scales a/U as $\mathrm{Pe} \to \infty$.

Short-time asymptotics and geometric skewness.—To better understand this behavior, we now present a new method to obtain general multiterm short-time asymptotics for arbitrary cross-sectional domains. For the first moment, assume an expansion $T_1(y,z,\tau) \sim (\tilde{T}_{1\tau}|_{\tau=0})\tau + (\tilde{T}_{1\tau\tau}|_{\tau=0})\tau^2/2$.

Matching gives $\tilde{T}_{1\tau}|_{\tau=0} = u(y,z)$ and $\tilde{T}_{1\tau\tau}|_{\tau=0} = \mathcal{L}(u)$. However, conservation of T_1 requires $\int_\Omega dydz T_1(y,z,\tau) = 0$ for all time. These initial coefficients violate conservation, since $\mathcal{L}(u) = 2p_x/\mu \neq 0$.

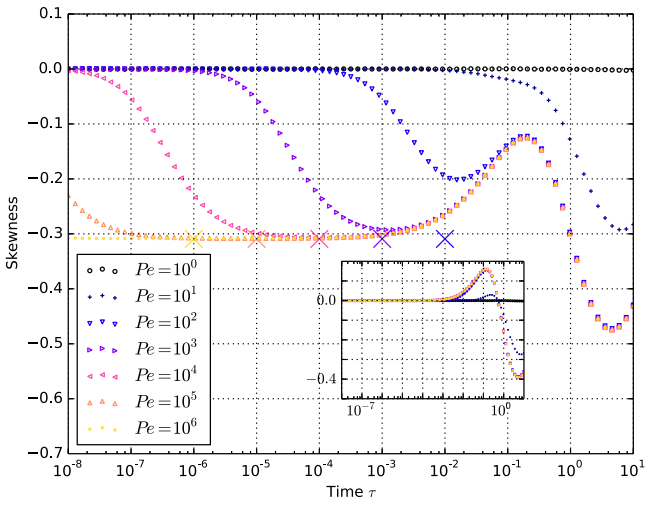

FIG. 3 (color online). Evolution of the full skewness for duct (pipe, inset), $\lambda = 1/5$, Péclet 10^0–10^6. The X's denote large Pe prediction of minima.

Subtracting $u\tau$ above from T_1 in Eq. (3) further reveals two Dirac-delta limiting sequences at the walls in a boundary layer of thickness $\sqrt{\tau}$. The quadratic term $\mathcal{L}(u)\tau^2/2$ survives in the interior, suggestive of Gaussian boundary layers at short time. Hence, these terms need to be incorporated to accurately capture the evolution. This provides a new method applicable to any geometry for generating short-time asymptotics, valid uniformly in space, for arbitrary moments.

Define the following Dirac-delta correction term (heat kernels for $\tau \to 0^+$), "stringing" them over $\partial\Omega$:

$$T_1(y,z,\tau) \sim u(y,z)\tau + [\mathcal{L}(u) - (\partial_{\mathbf{n}} u)\delta_b]\tau^2/2, \qquad (4)$$

with $\delta_b(\mathbf{y}) \equiv \int_{\partial\Omega} d\mathbf{y}' \delta(\mathbf{y} - \mathbf{y}')$ (outward normal $\mathbf{n}$). Integrating over the domain, the divergence theorem shows conservation is satisfied. The same process yields short-time asymptotics for T_2, T_3, $\mathcal{M}_2$, $\mathcal{M}_3$, and $\mathcal{M}_4$. The general short-time asymptotics for the full moments of Eq. (1), with Dirac-delta initial condition, are

$$\begin{aligned}
&\mathcal{M}_1 \sim 0, \quad \mathcal{M}_2 \sim 2\tau + \mathrm{Pe}^2\langle u^2\rangle\tau^2 + \frac{1}{3}\mathrm{Pe}^2\mathcal{L}(u)\langle\tilde{u}\rangle\tau^3,\\
&\mathcal{M}_3 \sim \mathrm{Pe}^3\langle u^3\rangle\tau^3 + \frac{1}{2}\mathrm{Pe}^3\mathcal{L}(u)(\langle\tilde{u}^2\rangle - 2\langle\tilde{u}\rangle^2)\tau^4,\\
&\mathcal{M}_4 \sim 12\tau^2 + 12\mathrm{Pe}^2\tau^3\langle u^2\rangle + \frac{1}{5}\mathrm{Pe}^4\tau^5\mathcal{L}(u)\langle u^3\rangle\\
&\qquad + \mathrm{Pe}^4\tau^4\langle u^4\rangle + \frac{1}{5}\mathrm{Pe}^4\tau^5\mathcal{L}(u)\langle\tilde{u}\rangle^3 - \frac{7}{5}\mathrm{Pe}^4\tau^5\langle u^2|\nabla u|^2\rangle\\
&\qquad + 4\mathrm{Pe}^2\tau^4\mathcal{L}(u)\langle\tilde{u}\rangle. \qquad (5)
\end{aligned}$$

These formulas agree with those in Ref. [2], once adjusted for the coordinate system. At large Pe, we find the skewness at short times determined solely by relative properties of Ω and uniform initial conditions (nonzero σ): $\mathcal{S}^{\mathcal{G}}_\sigma \equiv \mathcal{M}_3/\mathcal{M}_2^{3/2} = \langle u^3\rangle/[(\sigma/\mathrm{Pe}\tau)^2 + \langle u^2\rangle]^{3/2}$ [18] and $\mathcal{S}^{\mathcal{G}} = \lim_{\sigma\to 0}\mathcal{S}^{\mathcal{G}}_\sigma$.

The geometric skewness $\mathcal{S}^{\mathcal{G}}$ is independent of molecular diffusion. While there have been allusions to such flow effects for the special cases of channel or pipe flow [3,19,20], this concept has not been systematically developed nor have alternative geometries been considered. $\mathcal{S}^{\mathcal{G}}$ can be computed directly in the channel and circular or elliptical pipes, since u profiles are polynomials. In the channel, $\mathcal{S}^{\mathcal{G}} = -2\sqrt{5}/7$, while for elliptical pipes of *any* aspect ratio $\mathcal{S}^{\mathcal{G}} = 0$, as $\langle u^3\rangle = 0$ by direct integration of Ref. [14]. Conversely, the value for rectangular ducts ranges from the channel's value ($\lambda \to 0$), to *positive* ≈ 0.081169 for $\lambda = 1$.

Figure 4 shows the full-skewness evolution in ducts or ellipses for varying λ and the predicted first plateau values

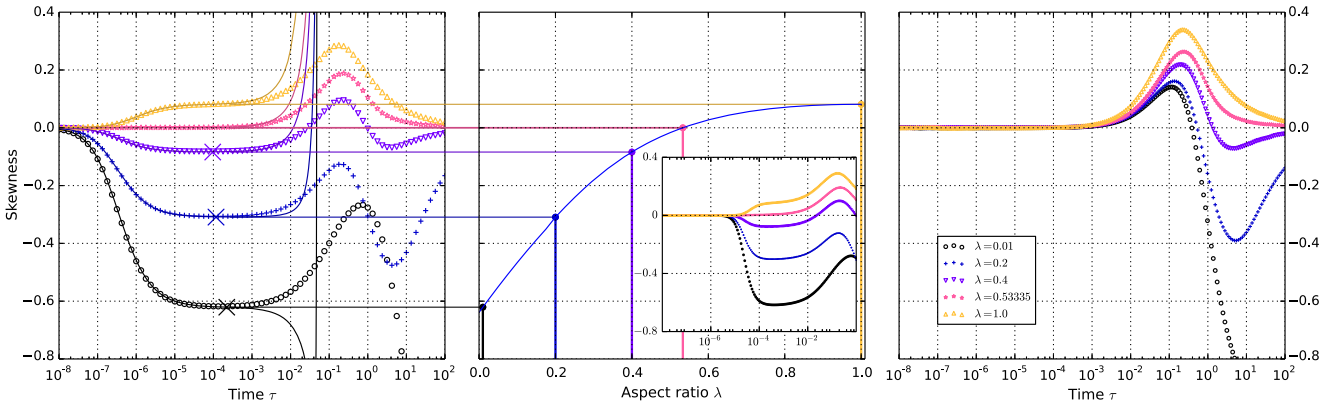

FIG. 4 (color online). Left: Full skewness evolution for ducts, $\lambda = 0.01$–1.0, $\mathrm{Pe} = 10^4$, short-time asymptotics (solid, vertical asymptote due to vanishing $\mathcal{M}_2$), Monte Carlo simulations (symbols). The X's denote asymptotic prediction of minima. Center: Duct $\mathcal{S}^{\mathcal{G}}$ vs λ, predicting first plateaus. Inset: Duct simulation, plug $f(x)$, $\sigma \approx 0.115$. Right: Ellipse full skewness, same parameters.

$\mathcal{S}^{\mathcal{G}}$. Remarkably, we observe at a "golden ratio" $\lambda^{\mathcal{G}} \approx 0.53335$, $\mathcal{S}^{\mathcal{G}}_{\sigma} \approx 0$, and this duct behaves similarly to the pipes. The inset shows a simulation with nonzero initial thickness. Inspection of $\mathcal{S}^{\mathcal{G}}_{\sigma}$ shows a scaling directly connecting different (σ^2, Pe) pairings producing identical dynamics by choosing larger Pe for larger σ^2. The inclusion of diffusion shows similar results for sufficiently large Pe, as analysis of the exact formulas (3) and simulations demonstrate. Different nondimensionalizations (e.g., fixed flux) link λ into the Péclet number definition, and the left panel would change because of the complicated (Pe, λ) landscape. Nonetheless, similar scaling relations as just discussed provide one-to-one mappings with the plots shown.

We remark that both pipes and ducts exhibit skewness sign changes for some aspect ratios. The question of sign definiteness, as for the circular pipe (positive) and the channel (negative), for other geometries is interesting. The second extrema in all duct simulations occur at time scales $t = ab/\kappa$ ($\tau = 1/\lambda$) for large Péclet number (the longer time scale b^2/κ presumably corresponds to the final inflection in skewness evolution). These second extrema are not purely flow induced; the physical mechanism derives asymmetry from a combination of tracer bending by the flow coupled with local regions of increased diffusive pumping, in a similar fashion to the heuristic arguments presented in Ref. [19]. This intuition predicts negative partial skewness in the interior and positive partial skewness near the boundaries. The duct and ellipse provide nontrivial interpolation between the limiting cases of channel and circular pipes.

The time scale of the critical value corresponding to geometric skewness can be predicted. Skewness critical points satisfy $\mathcal{M}_2\dot{\mathcal{M}}_3 - \frac{3}{2}\dot{\mathcal{M}}_2\mathcal{M}_3 = 0$. Short-time asymptotics yield the root-finding problem $c_3\tau^3 + c_2\tau^2 - \mathrm{Pe}^{-2}[c_1\tau + c_0] = 0$, with coefficients

$$c_0 = 36\langle u^3\rangle, \quad c_1 = 30\mathcal{L}(u)(\langle\tilde{u}^2\rangle - 2\langle\tilde{u}\rangle^2),$$
$$c_2 = 6\mathcal{L}(u)(\langle u^3\rangle\langle\tilde{u}\rangle - \langle u^2\rangle(\langle\tilde{u}^2\rangle - 2\langle\tilde{u}\rangle^2)),$$
$$c_3 = \mathcal{L}(u)^2\langle\tilde{u}\rangle(\langle\tilde{u}^2\rangle - 2\langle\tilde{u}\rangle^2). \tag{6}$$

Perturbative root-finding produces $\tau^* \sim \sqrt{c_0/c_2}\mathrm{Pe}^{-1}$ as $\mathrm{Pe} \to \infty$. In the channel, this gives $\tau^* \sim \sqrt{5/2}\mathrm{Pe}^{-1}$. Note c_0/c_2 is computationally observed to be positive for $\lambda \le \lambda^{\mathcal{G}}$ and becomes negative past this (there may be no extrema at this time scale). This quantitatively predicts the observed first minima in the figures, and in physical time, this is consistent with the time scale $t = a/U$.

Conclusion.—We have demonstrated new phenomena in the skewness evolution of a diffusing passive scalar by shear flows in various geometries. These include multiple extrema depending nontrivially upon the aspect ratio and Péclet number, as well as sign-indefinite skewness evolution connecting the strictly negative skewness in the channel with the strictly positive skewness in the circular pipe. In both geometries, the partial skewness varies with location, being always negative near the center and always positive near the boundaries on short time scales. New mathematical methods for computing the short-time asymptotics in arbitrary cross-sectional domains successfully predict the short-time evolution of the skewness and kurtosis, predicting the skewness' first plateau. The existence of similar plateaus in the partial skewness can be expected, possibly at different time scales. We remark that while the short-time asymptotics developed here successfully predict the first three partial moments, critical cancellations prevent accurate prediction of the partial skewness (hence, its plateaus) unless higher-order terms are retained. Similar effects may be considered in wall-driven as opposed to pressure-driven flows, as well as more complex geometries. Surprisingly, the geometric skewness in wall-driven pipe flows is nonzero, while the analogous

scenario in the channel is zero. Pressure-driven flows in more general geometries with $\mathcal{S}^{\mathcal{G}} \neq 0$ can be constructed by adding the real part of higher-order complex polynomials $P_n(y+\imath z)$ to the ellipse exact solution with zero level sets as boundary. The resulting typically smooth geometries show that $\mathcal{S}^{\mathcal{G}} \neq 0$ is unrelated to corners on the boundary.

We acknowledge funding received from the following National Science Foundation Grants No. RTG DMS-0943851, No. CMG ARC-1025523, and No. DMS-1009750.

*aminian@live.unc.edu
†bernardi@live.unc.edu
‡camassa@amath.unc.edu
§rmm@email.unc.edu

[1] G. Taylor, Proc. R. Soc. A **219**, 186 (1953).
[2] R. Camassa, Z. Lin, and R. M. McLaughlin, Commun. Math. Sci. **8**, 601 (2010).
[3] R. Smith, Q. J. Mech. Appl. Math. **35**, 345 (1982).
[4] P. C. Chatwin, J. Fluid Mech. **80**, 33 (1977).
[5] S. Vedel and H. Bruus, J. Fluid Mech. **691**, 95 (2012).
[6] W. N. Gill and R. Sankarasubramanian, Proc. R. Soc. A **316**, 341 (1970).
[7] C. V. D. Broeck, Physica (Amsterdam) **112A**, 343 (1982).
[8] N. Barton, J. Fluid Mech. **126**, 205 (1983).
[9] R. Camassa, R. M. McLaughlin, and C. Viotti, Phys. Fluids **22**, 117103 (2010).
[10] F. Gentile, M. Ferrari, and P. Decuzzi, Ann. Biomed. Eng. **36**, 254 (2008).
[11] W. Young and S. Jones, Phys. Fluids A **3**, 1087 (1991).
[12] R. Rusconi, J. S. Guasto, and R. Stocker, Nat. Phys. **10**, 212 (2014).
[13] R. Aris, Proc. R. Soc. A **235**, 67 (1956).
[14] With $U = a^2|p_x|/\mu$ and $\lambda = a/b$, the solutions to the flow problems in the channel, elliptical pipe, and rectangular duct are $\tilde{u}_{\text{channel}} = U[1-(y/a)^2]$, $\tilde{u}_{\text{duct}} = U\sum_{i,j=1}^{\infty} u_{ij}(\lambda)\phi_{ij}$, and $\tilde{u}_{\text{ellipse}} = U\{1/[2(1+\lambda^2)]\}[1-(y/a)^2-(z/b)^2]$, with $\phi_{ij} = \cos[(i-1/2)\pi y/a]\cos[(j-1/2)\pi z/b)]$.
[15] $\mathcal{P}_1(y,\tau) = \frac{y^4}{12} - \frac{y^2}{6} + \frac{7}{180}$, $\mathcal{P}_2(y,\tau;n) = 4[(-1)^n/(n\pi)^4]e^{-(n\pi)^2\tau}$,

$$\mathcal{Q}_1(y,\tau) = \frac{1}{226800}(-413 + 3840\tau - 1020y^2 + 3570y^4 - 2940y^6 + 675y^8),$$
$$\mathcal{Q}_2(y,\tau;n) = \frac{2(-1)^n}{(n\pi)^6}e^{-(n\pi)^2\tau}\left(\frac{17}{3} - \frac{64}{(n\pi)^2} - 2\tau + y^2\right),$$
$$\mathcal{Q}_3(y,\tau;n) = 4y\frac{(-1)^n}{(n\pi)^5}e^{-(n\pi)^2\tau}\left[-\frac{1}{(n\pi)^2} + \frac{1}{3}(y^2-1)\right]. \quad (7)$$

$$\mathcal{R}_1(y,\tau) = \frac{1}{30}\tau(7 - 30y^2 + 15y^4),$$
$$\mathcal{R}_2(y,\tau;n) = \frac{24(-1)^n}{(n\pi)^4}e^{-(n\pi)^2\tau}\tau,$$
$$\mathcal{R}_3(y,\tau;n) = (-1)^n e^{-(n\pi)^2\tau}\left[\frac{14640}{(n\pi)^{12}} - \frac{3705}{2(n\pi)^{10}} + \frac{691}{20(n\pi)^8} + \frac{3\tau^2}{(n\pi)^8} + y^2\left(-\frac{231}{2(n\pi)^{10}} + \frac{9}{2(n\pi)^8} - \frac{1}{3(n\pi)^6}\right) + y^4\left(\frac{23}{4(n\pi)^8} + \frac{2}{3(n\pi)^6}\right) - \frac{y^6}{3(n\pi)^6} + \tau\left(\frac{231}{(n\pi)^{10}} - \frac{31}{(n\pi)^8} - \frac{8}{15(n\pi)^6} - \frac{3y^2}{(n\pi)^8}\right)\right],$$
$$\mathcal{R}_4(y,\tau;n) = (-1)^n\frac{e^{-(n\pi)^2\tau}y}{(n\pi)^3}\left[\frac{231}{(n\pi)^8} + \frac{44}{(n\pi)^6} - \frac{28}{5(n\pi)^4} + y^2\left(-\frac{76}{(n\pi)^6} + \frac{4}{(n\pi)^4}\right) + \frac{8y^4}{5(n\pi)^4} + \tau\left(\frac{6}{(n\pi)^6} + \frac{2}{(n\pi)^4} - \frac{2y^2}{(n\pi)^4}\right)\right],$$
$$\mathcal{R}_5(y,\tau) = -\frac{4076777}{13621608000} + \frac{8447}{4989600}y^2 - \frac{713}{907200}y^4 - \frac{1}{1200}y^6 + \frac{13}{12096}y^8 - \frac{211}{453600}y^{10} + \frac{1}{14784}y^{12} + \frac{244}{155925}\tau - \frac{8}{945}\tau y^2 + \frac{4}{945}\tau y^4,$$
$$\mathcal{S}_1(\tau;n) = e^{-(n\pi)^2\tau}\frac{192}{(n\pi)^8}\tau,$$
$$\mathcal{S}_2(\tau;n) = e^{-(n\pi)^2\tau}\left(\frac{276096}{(n\pi)^{16}} - \frac{38560}{(n\pi)^{14}} + \frac{15488}{15(n\pi)^{12}} + \frac{3288}{(n\pi)^{14}}\tau - \frac{400}{(n\pi)^{12}}\tau - \frac{64}{15(n\pi)^{10}}\tau + \frac{24}{(n\pi)^{12}}\tau^2\right),$$
$$\mathcal{S}_3(\tau) = -\frac{32}{1575}\tau + \frac{64}{315}\tau^2,$$
$$\mathcal{S}_4(\tau) = \frac{7038848}{162820783125} - \frac{4352}{14189175}\tau + \frac{256}{297675}\tau^2. \quad (8)$$

[16] M. Matsumoto and T. Nishimura, ACM Trans. Model. Comput. Simul. **8**, 3 (1998).
[17] G. Marsaglia and T. A. Bray, SIAM Rev. **6**, 260 (1964).
[18] The value of $\mathcal{S}^{\mathcal{G}}$ may be calculated directly with $\kappa = 0$ using characteristics.
[19] P. C. Chatwin, J. Fluid Mech. **43**, 321 (1970).
[20] K. Jayaraj and R. S. Subramanian, Sep. Sci. Technol. **13**, 791 (1978).